Journal of Applied Physics

Identification of point defects on Co-Ni codoping in SnO_2 nanocrystals and their effect on the structural and optical properties

Cite as: J. Appl. Phys. **126**, 154303 (2019); https://doi.org/10.1063/1.5113479
Submitted: 04 June 2019 . Accepted: 04 October 2019 . Published Online: 17 October 2019

S. Roy, Brijmohan Prajapati, A. Singh, Amish G. Joshi, S. Chatterjee, and Anup K. Ghosh

Journal of Applied Physics ARTICLE scitation.org/journal/jap

Identification of point defects on Co-Ni codoping in SnO_2 nanocrystals and their effect on the structural and optical properties

Cite as: J. Appl. Phys. **126**, 154303 (2019); doi: 10.1063/1.5113479
Submitted: 4 June 2019 · Accepted: 4 October 2019 ·
Published Online: 17 October 2019

S. Roy,[1] Brijmohan Prajapati,[1] A. Singh,[2,a)] Amish G. Joshi,[3] S. Chatterjee,[4] and Anup K. Ghosh[1,b)]

AFFILIATIONS

[1]Department of Physics, Institute of Science, Banaras Hindu University, Varanasi 221005, India
[2]Central Instrument Facility, Indian Institute of Technology (Banaras Hindu University), Varanasi 221005, India
[3]CSIR-National Physical Laboratory, Dr. K. S. Krishnan Road, New Delhi 110012, India
[4]Department of Physics, Indian Institute of Technology (Banaras Hindu University), Varanasi 221005, India

[a)]**Present address:** Department of Condensed Matter Physics and Materials Science, Tata Institute of Fundamental Research, Mumbai 400005, India.
[b)]**Electronic mail:** akghosh@bhu.ac.in

ABSTRACT

$Sn_{0.97-y}Co_{0.03}Ni_yO_2$ ($0 \le y \le 0.04$) nanocrystals, with the average crystallite size in the range from 7.3 nm (for $y = 0.00$) to 5.6 nm (for $y = 0.04$), have been synthesized using a pH-controlled chemical coprecipitation technique. All the nonstoichiometric and stoichiometric point defects arising in the nanocrystals on codoping have been identified, and their effect on structural and optical properties of the nanocrystals have been extensively studied. It has been observed, using X-ray photoelectron spectroscopy (XPS), that on increasing the Ni codoping concentration (y), the nonstoichiometric Sn defect, Sn''_{Sn}, increases in compensation of the existing defect $Sn_i^{\cdots\cdot}$ for $y = 0.00$ nanocrystals. High-resolution transmission electron microscopy also confirms the existence of Sn''_{Sn}. Regarding the stoichiometric Frenkel defect, XPS results have indicated that the concentration of V_O and O_i, manifested in the form of dangling bond related surface defect states, increases with increase in y. Temperature dependent magnetization measurements of the nanocrystals confirm the charge state of V_O. The point defects have been found to affect the structural properties in a way that the distortion in the octahedral geometry of a complete Sn–O octahedron effectively reduces, whereas the distortion in the trigonal planar coordination geometry of oxygen increases. A direct effect of the O related Frenkel defect has been observed on the blue luminescence of the nanocrystals such that the spectral contribution of blue luminescence in the total emission intensity increases by ≈ 72% for $y = 0.04$ as compared to $y = 0.00$.

I. INTRODUCTION

Technologically important wide bandgap oxide semiconductors have attracted immense interest because of their diverse physicochemical properties and an ease of fabrication as compared to their traditional nonoxide counterparts.[1,2] Among them, SnO_2, because of its chemical stability, a large optical bandgap (≈3.6 eV), and n-type conductivity with a high carrier density (~10^{20} cm^{-3}), has been applied in a large range of device applications.[3–5]

SnO_2 is a IV–VI semiconductor. It crystallizes in the tetragonal rutile structure with space group $P4_2/mnm$, where each Sn(IV) ion is placed at the center of a slightly distorted oxygen octahedron and each O(II) ion is having trigonal planar coordination geometry with Sn(IV) ions.[6] SnO_2 possesses a unique coexistence of optical transparency (~ 97% of visible light) with high electrical conductivity, which is a rarity among materials.[7] This feature of SnO_2 originates from its inherent nonstoichiometry,[8–11] which in turn is due to its oxygen-related intrinsic point defects.[9,10,12] Many contradictory findings on the exact nature and origin of these defects have been reported so far. In one of the reports,[7] the oxygen deficiency in SnO_2 was attributed to Sn interstitials (Sn_i, as per Kröger-Vink notations[13]), which lowers the formation energy of oxygen vacancies (V_O) in the lattice. It was also concluded that Sn_i and V_O coexist

because of a strong mutual attraction (≈ 3.2 eV) between them. In another report, V_O was found to have lower formation energy than Sn_i, and the cluster defect of $Sn''_{Sn} + V_O^{\cdot\cdot}$ was calculated to be dominating because of their lowest formation energy (in O-rich conditions) and cause the overall oxygen deficiency in the lattice.[6] In some other reports, the cause of electrical conductivity of SnO_2 was attributed to incorporation of hydrogen impurities at interstitial sites or at lattice oxygen sites.[14–17] In a recent report, using a hybrid quantum mechanical/molecular mechanical (QM/MM) embedded cluster approach, it has again been shown that oxygen vacancies, forming deep states in SnO_2, contribute significantly to its intrinsic n-type conductivity.[18] However, most of these reports are based on first-principles calculations,[6,7,14,15,18] and proper conclusive experimental findings on the nature and composition of intrinsic defects of SnO_2 are scarcely available.[16,17] Recently, it has been shown, based on experimental results, that for $Sn_2(Nb_{2-x}Ta_x)O_7$ $(x = 0 - 2)$ — a multinary tin oxide-based transparent conducting oxide, controlling the lattice defects can help in tuning its optical bandgap and carrier density.[19] Thus, it can be assumed for SnO_2 that its intrinsic point defects can also have a profound effect on the structure and optical properties, a detailed study of which is lacking.

SnO_2 in pristine form is rarely used and dopants, such as Co,[20–22] Ni,[23–25] Cu,[5] Fe,[21] Mn,[26], etc., have been employed at the cationic site to tailor the physical and chemical properties. On doping, the transition metals form levels of *d*-electrons in the bandgap region of host SnO_2.[22,27] These localized *d*-electrons undergo interaction with the delocalized *s*- and *p*-electrons of host SnO_2, i.e., *sp-d* hybridization,[28] to yield interesting physical properties. Excellent optical and magnetic properties have been observed in Co doped SnO_2 nanostructures.[20,22,27,29–31] However, charge imbalance and ionic radius mismatch between dopant Co^{2+} (≈ 0.545 Å) and host Sn^{4+} (≈ 0.69 Å)[32] restrict the doping of Co at higher concentrations in SnO_2 nanocrystals.[22] Since the ionic radius of Ni^{2+} (≈ 0.69 Å) approximates to that of host Sn^{4+} (≈ 0.69 Å),[32] it can act as a better substitute.[33] In fact, Ni doped SnO_2 nanostructures have also shown some excellent optical and magnetic properties.[23,24] However, the number of available localized *d*-electrons for *sp-d* hybridization is effectively lower in the case of Ni than that for Co, when doped in SnO_2 nanocrystals. Moreover, both Ni and Co have been found to exist in mixed valence states as dopants in SnO_2 nanocrystals.[22,24] Thus, codoping Co and Ni in SnO_2 nanocrystals can simultaneously stabilize the structure of resulting nanocrystals; i.e., a higher doping concentration can be achieved, as well as multiple configurations of localized *d*-electrons can be built up in the band structure of the nanocrystals, leading to an improvement in the physical properties of the nanocrystals, as compared to those doped with only Co or Ni. For example, on doping Co in SnO_2 nanocrystals, it has been observed that the spectral contribution of UV emission and green emission toward the total emission for a particular nanocrystal has shown an increment with respect to the undoped nanocrystals whereas that for blue and violet emissions have shown a decrement on Co doping.[22] This renders the nanocrystals unsuitable for applications in blue LEDs, although SnO_2 possess a direct optical bandgap, considered as an essential feature for applications in blue LEDs.[34] Such limitations can be addressed by codoping Ni and Co in these nanocrystals.

Many reports on codoped SnO_2 nanocrystals, showing impressive optical, electrical, and magnetic properties, are available.[33,35–41] Based on the present literature for SnO_2 regarding the effect of intrinsic point defects on their physical properties, as discussed above, it can be well expected that, for transition metal codoped SnO_2 nanocrystals also, the optical, electrical, and magnetic properties would be influenced by the nature and concentration of the intrinsic point defects of the nanocrystals. In fact, relevant models, such as a bound magnetic polaron (BMP) model, which can successfully explain the origin of magnetism in these nanocrystals, necessitate the role of V_O, an intrinsic point defect, for explaining the observed magnetic properties.[42] Also, it is evident that there exists a relationship between the structural and other physical properties of transition metal doped SnO_2 nanocrystals.[43] The structural properties are dependent on the microstructural properties,[22,43–45] such as geometry of the Sn–O octahedron, etc., which in turn can be anticipated to be influenced by the nature and concentration of intrinsic point defects.[22] As such, an understanding of the formation of intrinsic defects and their effect on the structural geometry of Sn–O octahedron and other physical properties becomes very important. Few experimental reports concerning the identification and effect of point defects on physical properties in SnO_2 nanocrystals, doped with a single transition metal element, are available; for example, the identification and effect of point defects on the structural and optical properties have been extensively studied for Co doped SnO_2 nanocrystals,[22] the effect of anion Frenkel defects on the endurance behavior of Cu doped SnO_2-based memristors,[5] etc. However, convincing experimental reports regarding the effect on nature and concentration of intrinsic point defects on codoping with more than one transition metal element in SnO_2 nanocrystals are largely unavailable so far.

Here, we report on the identification of intrinsic point defects on Co and Ni codoping at the Sn site in SnO_2 nanocrystals and their effect on structural — from the viewpoint of the octahedral coordination geometry of Sn and the trigonal planar coordination geometry of O, and optical properties of the nanocrystals. To the best of our knowledge, this is the first experimental study for the identification and corresponding effect of intrinsic point defects on codoping cobalt and nickel at the Sn site in the SnO_2 nanocrystals. The results will help to understand the origin and nature of the optical, electronic, and magnetic properties of the codoped nanocrystals.

II. EXPERIMENTAL DETAILS

A. Synthesis

$Sn_{0.97-y}Co_{0.03}Ni_yO_2$ (with $0.00 \leq y \leq 0.04$) samples have been synthesized in an oxygen rich environment by salt hydrolysis of chloride precursors using the chemical coprecipitation method. The samples have been designated as SnO_2, and Ni0, Ni0.5, Ni2, Ni3, and Ni4 for nickel codoping concentration as $y = 0.00, 0.005, 0.02, 0.03,$ and 0.04, respectively. The synthesis procedure has been followed as reported earlier.[22] $NiCl_2{\cdot}6H_2O$ (HIMEDIA, min. assay = 97%) was used as a precursor for Ni in addition to the precursors for Sn ($SnCl_4{\cdot}5H_2O$; MOLYCHEM, min. assay = 98%) and Co ($CoCl_2.6H_2O$; HIMEDIA, min. assay = 99%), in stoichiometric amounts as per the codoping

concentration y, to prepare the 0.123 M homogeneous aqueous precursor solution. All other synthesis conditions have been kept the same as earlier.[22]

B. Characterization studies and measurements

1. Structural characterizations

The structural characterizations of the samples have been done using X-ray diffraction (XRD), transmission electron microscopy (TEM), and X-ray photoelectron spectroscopy (XPS). Room temperature X-ray diffractograms of the samples were recorded using a Miniflex II (Rigaku, Japan) X-ray diffractometer with Cu-K_α radiation ($\lambda = 1.5406$ Å) in Bragg-Brentano geometry. The loose powder samples were leveled on a sample holder for ensuring a smooth surface before recording the diffractograms. Low-resolution TEM, high resolution-TEM (HR-TEM), and selected area electron diffraction (SAED) measurements of the samples were carried out using a FEI Tecnai G^2 20 TWIN model (Japan) electron microscope. The samples were well dispersed in ethanol by ultrasonication for 15 min and then coated on a 300 mesh carbon-coated copper grid for the measurements. XPS (survey, Sn 3d core level, and O 1s core level) scans of the Ni0, Ni2, and Ni4 samples have been performed at room temperature using a monochromatic Al-K_α line at 1486.7 eV (300 W, 15 kV) from the Omicron multiprobe surface analysis system (Scienta Omicron GmbH), operating at an average vacuum of 2.5×10^{-9} Torr.

2. Study of optical properties

The effects of codoping on the optical properties of the samples were studied using reflectance spectroscopy and photoluminescence (PL) spectroscopy. The reflectance spectra of the samples were obtained at room temperature using a V750 (Jasco International, Inc., Japan) dual beam UV-Vis spectrophotometer. The spectra were collected in the wavelength range of 200–800 nm at 0.5 nm data intervals with a scan speed of 40 nm/min and 0.5 nm bandwidth. The response time of the photomultiplier tube (the detector) was kept at 0.96 s for the whole range of measurements. The PL emission spectra were collected at room temperature using a LS-45 (PerkinElmer, USA) fluorescence spectrometer. The samples were well dispersed in distilled water and excited at an excitation wavelength of 310 nm. The emission from the samples was scanned between 320 and 600 nm at a scan speed of 100 nm/min and a step scan of 0.5 nm.

3. Study of magnetic properties

The room temperature response of magnetization of the nanocrystals toward the applied magnetic field was studied using an EZ9 vibrating sample magnetometer (VSM; Microsense, USA). The powder samples of the nanocrystals were filled in acrylic cups, which were then mounted on a quartz sample holder for the measurements. Prior to each measurement, magnetization vs applied magnetic field data were recorded for blank acrylic cups, which were subtracted from the corresponding data of the samples for the necessary background corrections. The temperature dependent magnetization measurements for the Ni0 and Ni3 nanocrystals were done using a MPMS-03 (Quantum Design International, USA) SQUID magnetometer.

III. RESULTS

A. X-ray diffraction (XRD)

The XRD patterns of the nanocrystals, along with corresponding Rietveld refinements, are shown in Fig. 1. The XRD pattern of nanocrystalline SnO_2 (with an average crystallite size of 11.25 nm) is also shown in Fig. 1 for the sake of comparison. The Rietveld refinements were done using the EdPCR program (version 2.00) of FullProf Suite (version July 2017). The refinement data so obtained were used to calculate the structural parameters of the samples using the BondStr program (version July 2010) of FullProf Suite and VESTA (Visualization for Electronic and Structural Analysis, version 3.4.4). All the peak positions in Fig. 1 are indexed in accordance with JCPDS File No. 41-1445 for tetragonal SnO_2. From the refinement patterns, it can be observed that the $Sn_{0.97-y}Co_{0.03}Ni_yO_2$ nanocrystals are of single phase and correspond to the $P4_2/mnm$ space group of tetragonal cassiterite SnO_2.

The average crystallite size (D) and the average lattice strain(ε) developed in the nanocrystals on codoping have been calculated using size-strain plots (SSP),[46] represented by Eq. (1),

$$\left[\frac{d_{hkl}\beta^f \cos\theta_B}{\lambda}\right]^2 = \frac{0.9\lambda}{D}\left[\frac{d_{hkl}^2\beta^f \cos\theta_B}{\lambda^2}\right] + \left[\frac{\varepsilon}{2}\right]^2, \quad (1)$$

where d_{hkl} is the interplanar spacing, β^f is the full width at half maximum (FWHM) of structurally broadened profile (expressed in radians), θ_B is the Bragg angle, and λ is the wavelength of the Cu–K_α radiation used (1.5406 Å). d_{hkl} and θ_B are directly obtained from the Rietveld refinement of X-ray diffractograms of the nanocrystals, whereas β^f is calculated following a method described elsewhere.[22] Equation (1) can be framed into the equation of a straight line,

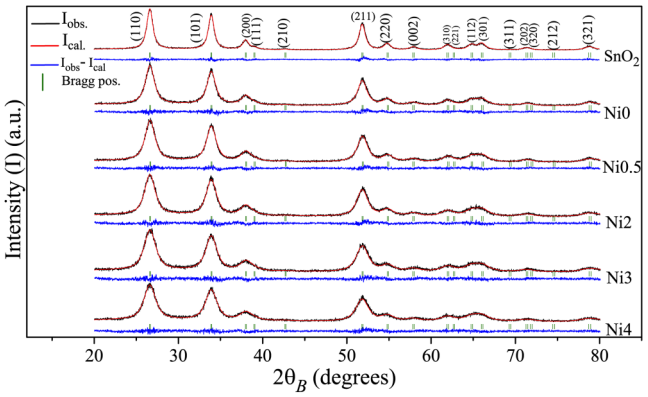

FIG. 1. XRD profiles, along with the Rietveld refinement, of the nanocrystals. The black lines correspond to the observed intensity ($I_{obs.}$), the red lines correspond to the calculated intensity ($I_{cal.}$), horizontal blue lines represent the difference between observed and calculated intensities ($I_{obs.} - I_{cal.}$), and the green vertical ticks correspond to the Bragg positions.

where the ordinate and abscissa are given by $y'_{SSP} = \left[\frac{d_{hkl}\beta^f \cos\theta_B}{\lambda}\right]^2$ and $x'_{SSP} = \left[\frac{d^2_{hkl}\beta^f \cos\theta_B}{\lambda^2}\right]$, respectively. Thus, the slope obtained from the linear fit of the SSP yields the average crystallite size (D) of nanocrystals and that the intercept yields the corresponding average lattice strain (ε) developed in the nanocrystal. Figure 2 shows the SSP, along with the linear fits, for the present $Sn_{0.97-y}Co_{0.03}Ni_yO_2$ nanocrystals by considering all the observed Bragg planes in Fig. 1 for each doping concentration. The variation of D with Ni concentration (y) is shown in Fig. 3, and the inset (a) shows the corresponding variation in ε. It can be observed that D exponentially decreases from ≈ 7.31 nm for Ni0 nanocrystals to ≈ 5.63 nm for Ni4 nanocrystals, with increase in Ni concentration (y); however, the corresponding variation of ε is quite linear and tensile in nature.

The lattice parameters $a(=b)$ and c for the $Sn_{0.97-y}Co_{0.03}Ni_yO_2$ nanocrystals have been obtained from the Rietveld refinement of the XRD profiles (Fig. 1). Figure 4 shows the variation of lattice parameters a and c with Ni concentration (y). It can be observed that with increase in y, a slightly increases [Fig. 4(a)] and c slightly decreases [Fig. 4(b)], with an increase in total volume $V(=a^2c)$ of the unit cell [Fig. 4(c)]. However, the observed qualitative variation in a is in contrary to an earlier report by Khan *et al.* for Co-Ni codoped SnO_2 nanoparticles, where a was found to decrease with increase in Ni codoping concentration.[39] A smaller ionic radius of dopants, Co^{2+} (≈ 0.65 Å) and Ni^{2+} (≈ 0.69 Å), as compared to the host Sn^{4+} (≈ 0.69 Å), was considered to be the reason for such a decrement in a with y. For the present nanocrystals, although the observed variation in lattice parameters with y is very small, a and c exhibit different qualitative responses toward increasing Ni concentration (y). Such behavior of a and c has been previously reported for SnO_2 nanostructures doped with a single dopant, such as Co,[22,43] Mn,[47] Fe,[44] etc. The observed results in such singly-doped SnO_2 nanocrystals were explained on the basis of ionic radii mismatch[22,44] and/or the difference in the oxidation state of the host and dopant,[43] or point defect induced structural distortions of the host lattice.[22,44] In fact, the role of intrinsic point defects of SnO_2 in the observed behavior of lattice parameters has been elaborately discussed for earlier Co doped SnO_2 nanocrystals[22] and has also been highlighted

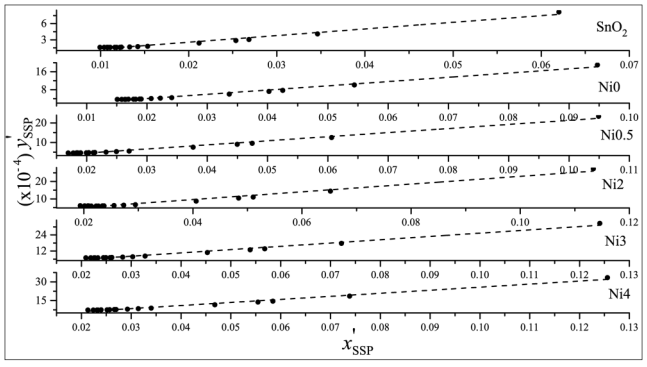

FIG. 2. Size-strain plot for the nanocrystals. The dotted lines represent the linear fits corresponding to the size-strain plots (SSP).

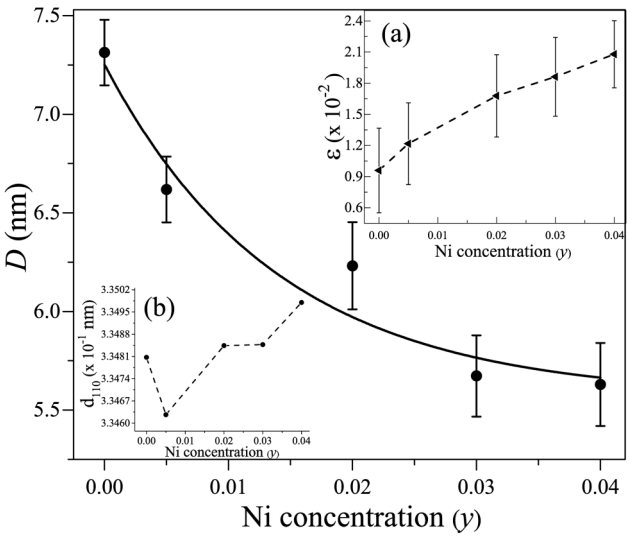

FIG. 3. The variation of average crystallite size (D) with Ni concentration (y) for the nanocrystals. The inset (a) shows the variation of average lattice strain (ε), and inset (b) shows the variation of d_{110} with Ni concentration (y). The solid line in the figure denotes the corresponding exponential fit and the dashed line is an eye guide.

for Co-Mn codoped SnO_2 nanoparticles,[40] although in the latter case, both a and c were observed to decrease with increase in codoping concentration. Hence, it can be safely assumed that codoping the SnO_2 nanocrystals with Co and Ni would influence the nature and concentration of intrinsic point defects of the host lattice, which in turn could impact the lattice parameters. Thus, the observed variation of lattice parameters in Fig. 4 for the present nanocrystals cannot be explained merely on the basis of difference in ionic radii of host and dopants and would require an in-depth understanding of the role of intrinsic point defects.

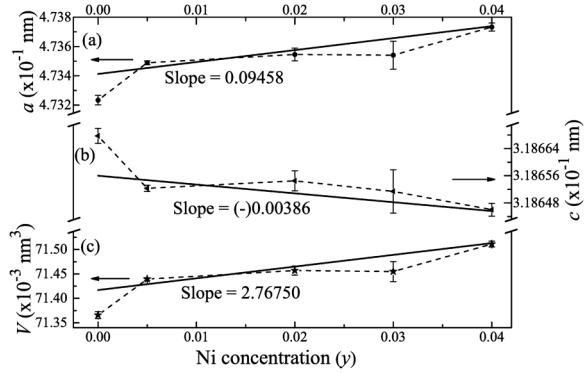

FIG. 4. The variation of the lattice parameter $a(=b)$ (a), c (b), and volume V (c) of the nanocrystals with Ni concentration (y). The solid lines, representing the corresponding linear fit, and the dashed lines serve as eye guides.

B. Transmission electron microscopy (TEM)

Transmission electron microscopy (TEM) provides a precise estimate of the morphology and microstructure of the nanocrystals. Figure 5(a) shows the bright-field low-resolution TEM images and the particle size distribution (bin size = 0.5 nm) for Ni3 nanocrystals. Most of the particles are spherical in shape and are in the size range of 6 nm–6.5 nm, with the most probable particle size (D_{TEM}) around 6.25 nm. This corroborates the average crystallite size (D) (Fig. 3) as estimated from the X-ray diffractogram of the nanocrystals.

Selected area electron diffraction (SAED) patterns are considered to give a better insight into the crystalline nature of nanocrystals. Circular ringlike patterns of very closely spaced bright spots are observed from the SAED pattern of the Ni3 [Fig. 5(b)], which indicates a good crystallinity of the nanocrystals. Indexing of the SAED patterns [Fig. 5(b)] corresponds to the same order of lattice planes as obtained from the Rietveld refinement of the X-ray diffractogram of the nanocrystals; i.e., they match well with that of the tetragonal SnO_2 phase.

For having a view of the atomic arrangement in the nanocrystals, high-resolution TEM (HR-TEM) of the nanocrystals has been performed, as shown in Fig. 5(c). Intertwined atomic planes can be observed, which indicates the presence of more than one type of atomic arrangement in the nanocrystals. From Fig. 5(c), four typical sets of atomic planes have been identified—with interplanar spacings (d_{hkl}) of 3.310 Å (Region I), 3.324 Å (Region II), 3.191 Å (Region III), and 3.115 Å (Region IV). The d_{hkl} of ≈ 3.3 Å (corresponding to Regions I and II) matches with that of d_{110} of the Ni3 nanocrystals as obtained from the Rietveld refinement (d_{110} = 3.348 07 Å) considering the tetragonal SnO_2 phase (JCPDS No. 41-1445), where Sn is in the +4 oxidation state. The d_{hkl} of ≈ 3.1 Å (corresponding to Regions III and IV) does not match with any (hkl) value of tetragonal SnO_2; however, they match with that of {112} planes of the orthorhombic SnO phase (JCPDS No. 77-2296), where Sn is in the +2 oxidation state. Thus, contrary to diffraction results, HR-TEM indicates formation of some local structures resembling SnO in the overall tetragonal SnO_2 lattice of the nanocrystals. This contradiction to diffraction results is expected since the average particle size of the nanocrystals is very small (≈ 6.25 nm); in addition, with not-so-good crystallinity of the nanocrystals, the diffraction patterns cannot provide accurate structural information for the nanocrystals.[48,49]

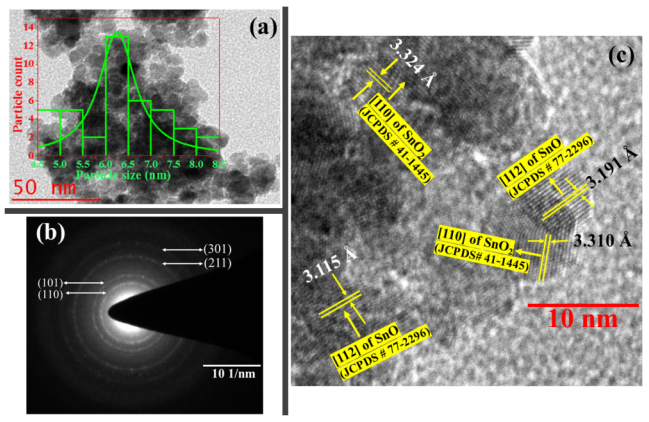

FIG. 5. Bright-field low-resolution TEM (a), SAED pattern (b), and HR-TEM image (c) of the Ni3 nanocrystals.

C. X-ray photoelectron spectroscopy (XPS)

Room temperature XPS study of the nanocrystals can be useful to determine the elemental composition as well as electronic states of Sn and O in the samples. All the observed peak positions, along with the obtained spin–orbit splittings (SOS), in the XPS survey and core-level scans of the present nanocrystals have been indexed from the National Institute of Standards and Technology (NIST) XPS database.[50] The experimental peak area values were first divided by the number of sweeps to get the atomic areas, which were then divided by the respective atomic scattering factors (ASF) for the quantitative analysis of the samples. The C 1s signal at 284.5 eV has been used as the standard for calibrating the spectral positions to account for sample charging effects.

The XPS survey scans for the Ni0, Ni2, and Ni4 nanocrystals are shown in Fig. 6. The observed peaks confirm the presence of Sn, O, Co, and Ni in the nanocrystals and that the nanocrystals do not have an admixture of any other element.

The core-level XPS spectra of Sn 3d (Fig. 7) show the presence of Sn 3d doublets $3d_{3/2}$ and $3d_{5/2}$ centered at around 494.7 eV and 486.3 eV, respectively. Clear asymmetry in the peaks for Ni0 and Ni2 nanocrystals can be observed, indicating the presence of more than one peak in each region. To clarify it, the Sn 3d doublets have been deconvoluted (Fig. 7). It can be observed that the deconvolution of the Sn $3d_{5/2}$ peak leads to two peaks for Ni0 and three peaks for Ni2 nanocrystals. The best deconvolution results have been obtained with a spin–orbit splitting (SOS) value of 8.4 eV for both the deconvoluted peaks of $3d_{5/2}$ in the case of Ni0. For Ni2, best deconvolution is obtained with an SOS of 8.5 eV for the peak

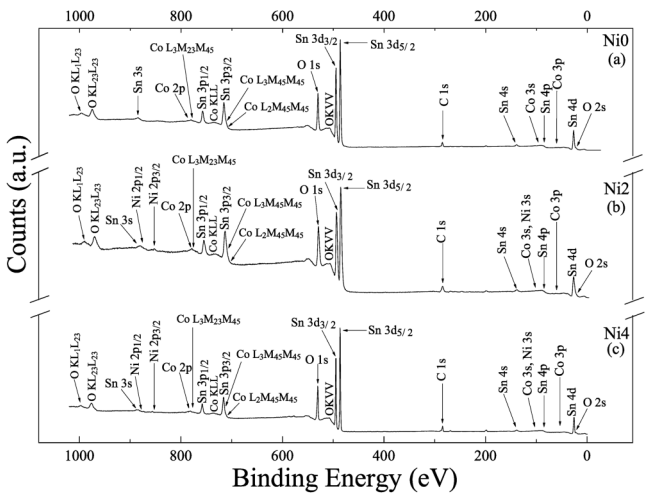

FIG. 6. Room temperature survey scan XPS spectra of the nanocrystals.

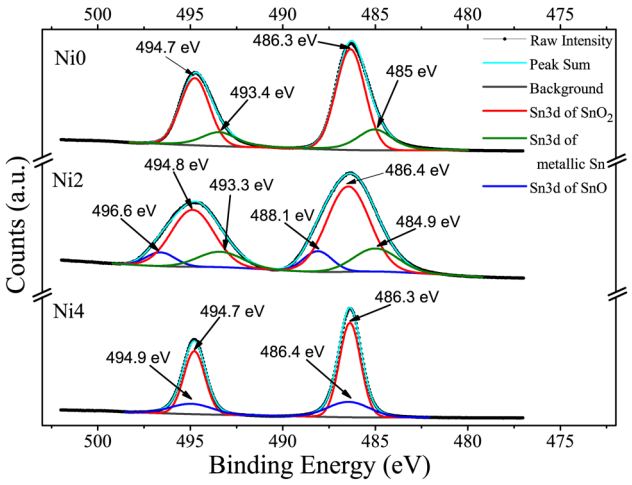

FIG. 7. Room temperature Sn 3d core-level XPS spectra of the nanocrystals.

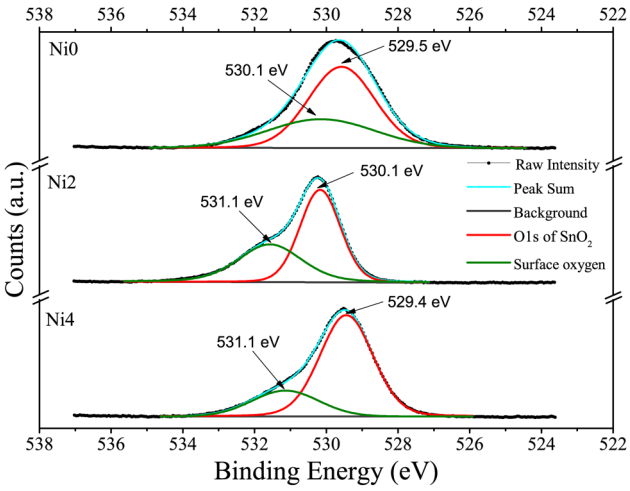

FIG. 8. Room temperature O 1s core-level XPS spectra of the nanocrystals.

with the highest binding energy (BE) and an SOS of 8.4 eV for the two peaks with the lower BEs. For Ni0, it is observed from Fig. 7 that one of the deconvoluted peaks corresponds to the BE of 486.3 eV in the $3d_{5/2}$ region and 494.7 eV in the $3d_{3/2}$ region. Similar peaks for Ni2 lie at BEs of 486.4 eV and 494.8 eV (Fig. 7). From the observed BE and SOS of 8.4 eV, the peaks can be assigned to lattice Sn of SnO_2.[50] Upon careful examination of the $3d_{5/2}$ peak at 485 eV for Ni0 and at 484.9 eV for Ni2 nanocrystals (Fig. 7), both with an SOS value of 8.4 eV, it can be found that it corresponds to that of Sn in the metallic state.[50] Furthermore, the $3d_{5/2}$ peak at 488.1 eV for Ni2 is obtained on deconvolution with an SOS value of 8.5 eV (Fig. 7), which is only assigned to Sn 3d of SnO.[50] Hence, this peak can be assigned to the +2 oxidation state of Sn in SnO. In the case of Sn 3d core-level spectra for Ni4 nanocrystals (Fig. 7), although both the $3d_{5/2}$ and $3d_{3/2}$ peaks appear symmetric, deconvolution procedure, similar to the Ni0 and Ni2, is adopted to check the presence of more than one peak in the $3d_{5/2}$ and $3d_{3/2}$ regions (Fig. 7). It can be observed that the deconvolution yields two peaks in both the regions, with best results obtained using SOS of 8.4 eV and 8.5 eV for the deconvoluted peaks having higher and lower counts, respectively. However, the BE separation between the deconvoluted peaks in either region is of only 0.1 eV, which is much lower as compared to the resolution of the hemispherical analyzer, which is 0.6 eV. As such, no such asymmetry can be noticed, which can indicate the presence of convoluted peaks in the spectra. However, the deconvoluted peak with lower count has an area spread outside to that of the deconvoluted peak with higher counts; thus, the deconvolution process has led to a division of a peak area (and not merely division of counts) under each of the convoluted peak, confirming the presence of more than one peak in each region. From the SOS values, the deconvoluted peaks with higher and lower counts in either region can be assigned to lattice Sn of SnO_2 and to the +2 oxidation state of Sn in SnO.[50] The small difference of BE of the two deconvoluted peaks is expected as the BE spread of the Sn $3d_{5/2}$ peak in SnO and SnO_2 overlaps for a significant energy range.[51] With Ni concentration, no conclusive chemical shift for any of the Sn 3d peaks (Fig. 7) has been observed.

The O 1s core-level XPS spectra (Fig. 8) show the presence of a O 1s singlet peak centered at ≈ 529.8 eV for the nanocrystals. A clear asymmetric broadening of the peak on the higher BE side has been observed for all the nanocrystals. Deconvolution of the peak yields two symmetric peaks centered at 529.5 eV and 530.1 eV for Ni0, at 530.1 eV and 531.1 eV for Ni2, and at 529.4 eV and 531.1 eV for Ni4. The peak at ≈ 529.5 eV can be assigned to lattice O in SnO_2.[50] Also, there is no significant change in the BE value of this peak with Ni codoping concentration (y). The peak at ≈ 530.1 eV is assigned to the surface dangling bond states (E_s) resulting from the species, such as O_2^{2-} and O^-.[22]

D. Reflectance spectroscopy

Reflectance spectroscopy is an important tool to study optical absorption processes in semiconductor nanocrystals, which conveys important information, such as the nature of optical transitions (direct or indirect), the optical bandgap, and lattice imperfections. The reflectance spectra of the $Sn_{0.97-y}Co_{0.03}Ni_yO_2$ nanocrystals as a variation of incident photon wavelength (λ) are shown in Fig. 9. In its bulk state, SnO_2 is a direct bandgap semiconductor.[52] Due to the presence of an inversion center symmetry in the ideal SnO_2 crystals, however, the band to band edge transitions are of forbidden nature due to the even parity symmetry of the band edge quantum states.[53] It has been reported that reducing the size of SnO_2 crystals to the nanoregime, inducing defects by doping, etc., can modify the symmetry of the band edge quantum states such that the forbidden nature of direct optical transitions can be suppressed partially or completely.[4] The direct allowed bandgap ($E_g^{allw.}$) for each nanocrystal has been calculated from its reflectance spectrum using Tauc's plot.[54] The existence of direct allowed transitions in the nanocrystals establishes a modification of the symmetry of

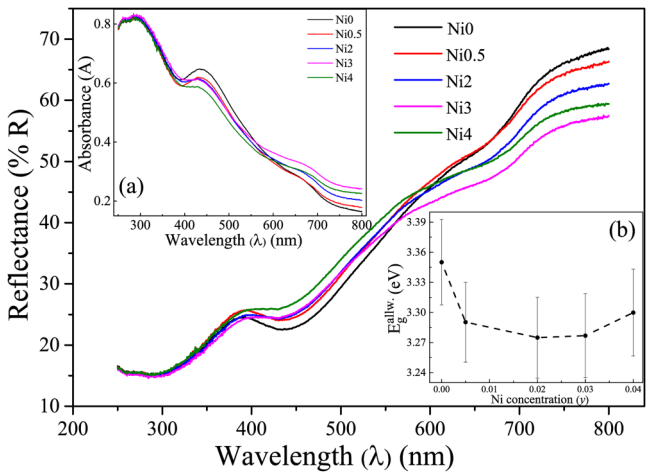

FIG. 9. Room temperature reflectance spectra of the nanocrystals. The inset (a) of the figure represents the corresponding absorbance spectra of the nanocrystals, whereas the inset (b) of the figure shows the variation of the allowed optical bandgap ($E_g^{allw.}$) of the nanocrystals with Ni concentration (y), the dashed line being served as an eye guide.

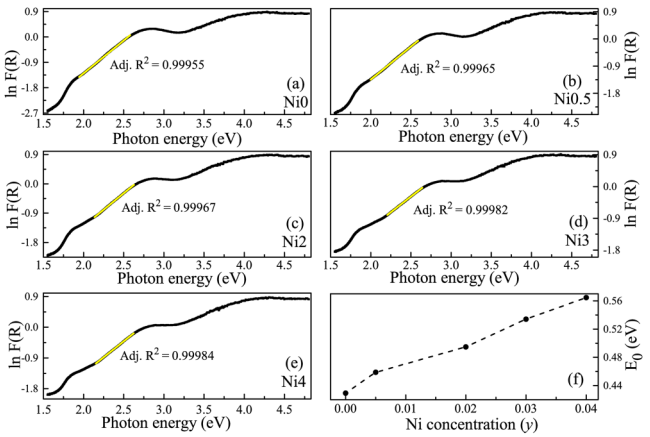

FIG. 10. The plots for Urbach-type absorption [according to Eq. (2) in the nanocrystals] (a)–(e) and variation of the E_0 with Ni concentration (y) (f). The solid yellow lines in (a)–(e) represent the corresponding linear fits, whereas the dotted line in (f) is for an eye guide.

the band edge quantum states. This symmetry modification has also been reported earlier for Co doped SnO_2 nanocrystals.[22] The variation of $E_g^{allw.}$ with y is shown in the inset (b) of Fig. 9. The optical bandgap of the nanocrystals first decreases with increasing y up to $y = 0.02$ and then increases thereafter. This is different from the earlier observation for only Co doped SnO_2 nanocrystals,[22] where a red shift of the bandgap has been observed throughout the Co doping concentration, confirming the effect of Ni codoping with Co on the optical bandgap modification of the SnO_2 nanocrystals.

Additionally, an exponential edge, i.e., the Urbach edge,[55] has also been observed near the optical band edge in the reflectance spectra of the nanocrystals. The Urbach-type absorption is represented by[54,56–58]

$$\alpha(h\nu) = \alpha_0 \exp\left[\gamma\left\{\frac{h\nu - h\nu_0}{k_B T}\right\}\right], \quad (2)$$

where $\alpha(h\nu)$ is the absorption coefficient of the nanocrystals at an incident photon energy $h\nu$ and α_0, γ, and $h\nu_0$ are fitting parameters and material-dependent. The empirical parameter $\frac{k_B T}{\gamma}$ has the dimensions of energy. From Eq. (2), it can be shown that[56]

$$E_0 = \left[\frac{d(\ln(\alpha))}{d(h\nu)}\right]^{-1}, \quad (3)$$

where $E_0 = \frac{k_B T}{\gamma}$. Substituting the Kubelka-Munk function [F(R)] for α in Eq. (3) [since F(R) is proportional to $\alpha(h\nu)$], we have

$$E_0 = \left[\frac{d(\ln(F(R)))}{d(h\nu)}\right]^{-1}. \quad (4)$$

The plots of ln F(R) vs $h\nu$ for the present nanocrystals [Figs. 10(a)–10(e)] yield straight lines for photon energies below the optical bandgap of the nanocrystals, confirming the Urbach-type absorption.[55] This Urbach-type absorption occurs when the electronic density of states exponentially tail into the bandgap region owing to various structural disorders in the lattice of the semiconductors.[58] The empirical parameter E_0 describes this distribution of the density of states and is correlated with impurity concentration responsible for disorder in crystallinity of the nanocrystals, leading to the Urbach edge.[56,57] Urbach type absorption has also been found earlier for SnO_2-based nanostructures[3,29,59] as well as for other semiconductors.[57] In fact, a strong Urbach-type absorption has been observed for Co doped SnO_2 nanocrystals reported earlier[22] and was found to be pronounced on Co doping. E_0 for the present nanocrystals has been calculated as, according to Eq. (4), from the inverse of the slope of the straight lines in Figs. 10(a)–10(e) and its variation with Ni codoping concentration (y), which is shown in Fig. 10(f). On codoping Ni with Co, E_0 increases, indicating an enhancement of structural disorders in lattice of the SnO_2 nanocrystals because of codoping.

E. Photoluminescence (PL) spectroscopy

Photoluminescence (PL) spectroscopy is a nondestructive spectroscopic technique useful for studying the presence and corresponding effect of various intrinsic and extrinsic point defects in semiconductor nanocrystals. The fluorescence PL spectra of the present nanocrystals is shown in Fig. 11. The observed PL spectra are divided into four spectral regions — ultraviolet (UV) (below 380 nm), violet (380 nm–450 nm), blue (450 nm–490 nm), and green (490–560 nm) emissions. The presence of these emission peaks at energies corresponding to the sub-bandgap region indicates the presence of various point defect related energy levels in the forbidden zone, acting as

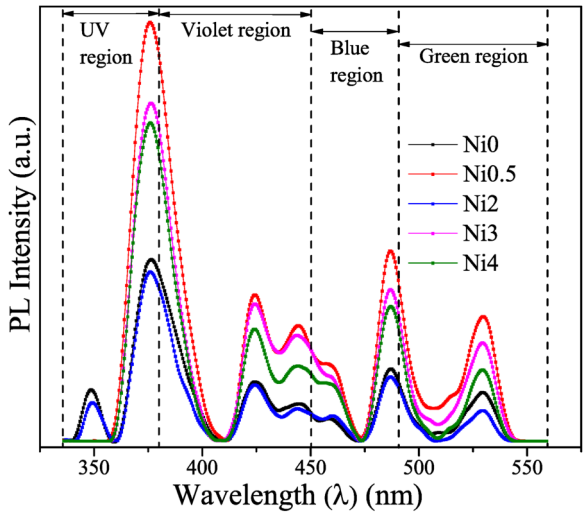

FIG. 11. Room temperature PL spectra of the nanocrystals.

recombination levels for electrons relaxing from the conduction band to the valence band.

In the earlier report for Co doped SnO_2 nanocrystals, it was observed that the spectral contribution of UV and green emissions, in the total emission from a nanocrystal, has shown an increment for the Co doped nanocrystals with respect to the undoped nanocrystals whereas that for the blue and violet emissions have shown a decrement on Co doping.[22] Now, for SnO_2 nanocrystals, the UV emission is affected by the parity of its band edge quantum states,[4,22] whereas the blue and green emissions are affected by the concentration of its oxygen-related intrinsic point defect levels.[22,60–62] Since the present study deals with the effect of codoping SnO_2 nanocrystals with Co and Ni on its intrinsic point defects, here the corresponding effect on the spectral contribution of blue and green emissions is discussed in detail. To obtain the spectral contribution of blue and green emissions from a nanocrystal toward its total emission, all the observed PL emission peaks in Fig. 11 have been deconvoluted, using Gaussian function [Eq. (5)],

$$I = \frac{A}{\sqrt{2\pi}\beta}\exp\left[\frac{-1}{2}\left(\frac{\lambda-\lambda_0}{\beta}\right)^2\right], \tag{5}$$

where I is the observed PL intensity, λ is the emitted photon wavelength, A is the area under the emission peaks, λ_0 is the obtained emission peak positions on the wavelength scale, and β is the emission peak width. The parameters so obtained are listed in Table S1 of the supplementary material. The area under the deconvoluted emission peaks (A) in each spectral region, obtained using Eq. (5) for a particular Ni concentration, was added to get the total strength of the PL emission (A_R) corresponding to the spectral region, from this Ni concentration. All the A_R corresponding to each spectral region are then added, which yields the strength of total PL emission (A_T) from the nanocrystal with the specific Ni concentration. The

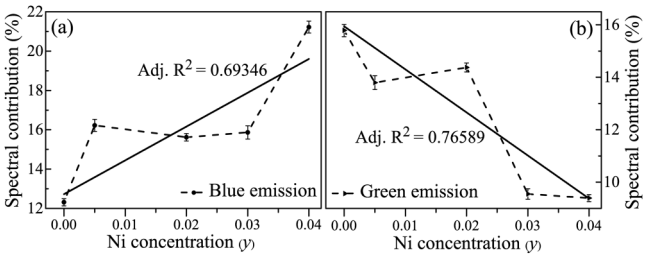

FIG. 12. The variation of spectral contribution (%) of blue emission (a) and green emission (b) in the total emission spectra of the nanocrystals, with Ni codoping concentration (y). The solid lines are linear fits and the dotted lines are eye guides.

spectral contribution percentage for blue and green emissions in the total emission spectrum for a y is then calculated by taking the ratio of respective A_R with the A_T for this Ni concentration. Figure 12 shows the variation of spectral contribution of the blue and green emissions to the total emission spectra for a nanocrystal with the Ni codoping concentration (y). It can be observed that the spectral contribution of blue luminescence [Fig. 12(a)] shows a remarkable enhancement by $\approx (72.33 \pm 0.98)\%$ for Ni4 with respect to Ni0 nanocrystals, whereas the corresponding spectral contribution for green emission [Fig. 12(b)] has decreased by $\approx (40.49 \pm 0.75)\%$. Thus, a significant improvement is achieved in blue luminescence on codoping the $Sn_{0.97}Co_{0.03}O_2$ nanocrystals ($y = 0.00$) with Ni.

F. Magnetic property

The variation of magnetization (M) with the applied magnetic field (H) at 300 K for the present nanocrystals is shown in Fig. 13. Pure SnO_2 nanocrystals exhibit diamagnetism, as evident from the black curve in Fig. 13. However, on codoping with Ni and Co, the M-H behavior of the nanocrystals seems to exhibit paramagnetism at 300 K. This is in contrary to an earlier report by Khan *et al.*,[39] where they have observed ferromagnetism at 300 K for the Co and Ni codoped SnO_2 nanoparticles throughout the Ni concentration. However, different synthesis conditions were used by Khan *et al.* for preparing the codoped nanoparticles with 5 at. % Co and varying Ni concentration, as compared to that adopted in the synthesis of the present $Sn_{0.97-y}Co_{0.03}Ni_yO_2$ nanocrystals. Now, dissimilar synthesis conditions can affect the structural properties differently, as is also evident by the contrary variation in the lattice parameter a (in Fig. 4) for the present nanocrystals in comparison with this earlier report by Khan *et al.* Since the structural and other physical properties of transition metal doped SnO_2 nanocrystals are related,[43] hence, the observed difference in the magnetic behavior can be expected.

To confirm the dominant magnetic interactions in the nanocrystals below 300 K, magnetization (M) as a function of temperature (T) of the nanocrystals is studied at an applied magnetic field of 500 Oe. The resulting variation of inverse susceptibility (χ^{-1}) with temperature (T) is shown in the inset of Fig. 13. Now, a system, above a magnetic ordering temperature, is expected to follow the

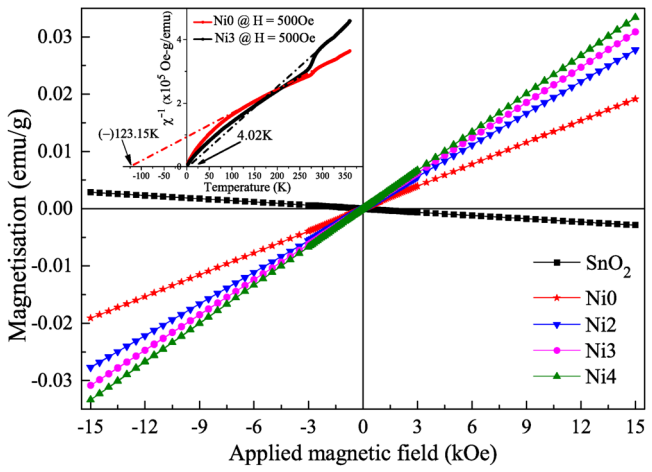

FIG. 13. Room temperature response of the magnetization (M) toward the applied magnetic field (H) for the nanocrystals. The inset figure shows the temperature dependent magnetization (M) curves for the Ni0 and Ni3 nanocrystals. The dashed-dot lines in the inset figure represents the corresponding Curie-Weiss fits.

Curie-Weiss law [Eq. (6)],

$$\chi = \frac{C}{T - \Theta}, \tag{6}$$

where C is the Curie constant and Θ is the Curie-Weiss temperature. Thus, a plot of χ^{-1} vs T, i.e., Eq. (7),

$$\chi^{-1} = \frac{T}{C} - \frac{\Theta}{C}, \tag{7}$$

is expected to give a linear region in the high temperature range with a zero, negative, and positive intercept on the χ^{-1}-axis for the dominant paramagnetic, ferromagnetic, and antiferromagnetic interactions, respectively, in the system. From the inset of Fig. 13, it can be seen that a linear region exists in the high temperature range of 290 K–360 K for both the Ni0 and Ni3 nanocrystals, conforming to the Curie-Weiss law. The linear fit using Eq. (7) for the nanocrystals yields a positive intercept with $\Theta \approx (-)123.15$ K for Ni0, whereas that for Ni3, a negative intercept is obtained with $\Theta \approx 4.02$ K. The observed $\Theta \approx (-)123.15$ K for Ni0 nanocrystals indicates the presence of dominant antiferromagnetic interactions below 290 K in the nanocrystals, and a $\Theta \approx 4.02$ K in Ni3 suggests that the nanocrystals are ferromagnetic below 290 K. This conversion from antiferromagnetic interactions to ferromagnetic interactions below 290 K suggests the inclusion of paramagnetic centers in the lattice of the nanocrystals because of codoping. However, the exact origin of magnetic interactions in the nanocrystals needs to be investigated further.

IV. DISCUSSION

The effect of codoping Ni with Co on *D* and lattice of the $Sn_{0.97-y}Co_{0.03}Ni_yO_2$ nanocrystals is clearly observed from Figs. 3 and 4, respectively. The exponential decrease in *D* (Fig. 3) with increase in *y* can be attributed to growth kinetics involved during the nucleation process of the nanocrystals.[22] The decrease in *D* is such that after $y = 0.02$, *D* transitions from the weak confinement region (Bohr exciton radius for SnO_2 ≈2.5 nm) to the strong confinement region, which is marked by a blue shift in $E_g^{allw.}$ after $y = 0.02$ [the inset (b) of Fig. 9]. Now, in an ideal tetragonal SnO_2, with space group $P4_2/mnm$, Sn^{4+} is located at the 2a lattice site in distorted octahedral coordination geometry with O^{2-} at the 4f position, and each O^{2-} in turn has a trigonal planar coordination geometry with Sn^{4+}.[7] When Co and Ni are doped at the cationic site in SnO_2, they can have either +2 or +3 as a possible charge state.[22,24] Hence, when Co and Ni are codoped at the 2a lattice site of Sn in SnO_2, there would be lowering of positive charge at more number of lattice sites as compared to only Co doped SnO_2 nanocrystals; i.e., charge neutrality condition would tend to be violated, much pronounced than as compared to only for Co doped SnO_2 nanocrystals reported earlier.[22] Also, the ionic radii of Co in octahedral geometry (assuming in low spin configuration) are 0.65 Å (for Co^{2+}) and 0.545 Å (for Co^{3+}) and those for Ni are 0.69 Å (for Ni^{2+}) and 0.56 Å (for Ni^{3+}), whereas the ionic radius of Sn^{4+} is 0.69 Å.[32] Thus, when Co and Ni are codoped in SnO_2 nanocrystals, due to violation of charge neutrality condition as well as ionic radius mismatch, the tetragonal crystal symmetry of the nanocrystals would tend to be broken down. However, from Fig. 1, it can be observed that the $Sn_{0.97-y}Co_{0.03}Ni_yO_2$ nanocrystals retain the $P4_2/mnm$ space group of tetragonal SnO_2 throughout the entire range of the Ni doping concentration. Thus, it can be expected that to maintain the tetragonal crystal symmetry, some other factors, such as intrinsic point defects, must play a counteractive role. It is evident from Fig. 4 that for the present nanocrystals, although the observed quantitative variation in lattice parameters with *y* is very small, *a* and *c* exhibit different qualitative responses toward increasing Ni concentration (*y*). Thus, it becomes evident that simply considering the difference between the ionic radii of the dopants and host cannot explain the structural changes induced in the nanocrystals due to codoping and needs a different perspective, for example, the effect on configuration of intrinsic point defects by codoping. In the earlier report for Co doped SnO_2 nanocrystals,[22] where exact same synthesis conditions have been used to prepare the nanocrystals, it was found that on increasing the Co doping concentration, the concentration of intrinsic point defects, tin interstitials, increased and that of oxygen vacancies decreased, which modified the lattice parameters of the Co doped SnO_2 nanocrystals.[22] Thus, a change in the configuration of intrinsic point defects on codoping with Ni in the nanocrystals can be expected, which in turn can modify the structural and other physical properties of the present nanocrystals.

A. Identification of point defects

First-principles density functional theory calculations for SnO_2 have indicated that nonstoichiometric defects have lower formation energies than stoichiometric defects and hence would dominate the resulting defect structure.[6] Thus, for the present nanocrystals, the presence of nonstoichiometric defects can be expected.

1. Nonstoichiometric defect

As stated above, in an ideal crystal lattice of SnO_2, Sn^{4+} is situated at 2a lattice sites in distorted octahedral coordination

geometry with O^{2-}, located at 4f sites. These Sn^{4+} at 2a sites and O^{2-} at 4f sites, being charge neutral with respect to the original lattice, can be designated as Sn^{x}_{Sn} and O^{x}_{O}, respectively, in accordance with Kröger-Vink notations.[13] The existence of Sn^{x}_{Sn} in the present $Sn_{0.97-y}Co_{0.03}Ni_yO_2$ nanocrystals is evident from the occurrence of the most intense Sn $3d_{5/2}$ core-level peak at ≈ 486.3 eV (Fig. 7), and the occurrence of the O 1s core-level peak at ≈ 529.2 eV (Fig. 8) confirms the presence of O^{x}_{O} in the nanocrystals. As can be seen from Fig. 7, for the Ni0 and Ni2 nanocrystals, a Sn $3d_{5/2}$ core-level peak corresponding to metallic Sn has appeared on the lower binding energy side to Sn^{x}_{Sn} at around 485 eV for Ni0 and 484.9 eV for Ni2 nanocrystals. From the BE and SOS of this peak,[50] it can be assigned to Sn going to an interstitial site, i.e., Sn_i. Now, charge neutral Sn_i requires a much higher formation energy than Sn_i in the +4 charge state for it to be placed in the SnO_2 lattice.[7] Hence, the corresponding point defect can be identified as $Sn_i^{\cdots\cdot}$. This is a nonstoichiometric interstitial Sn defect, which has been predicted, based on first-principles calculations, to be a stable defect in SnO_2[7] and has also been observed earlier for Co-doped SnO_2 nanocrystals.[22] However, the point defect $Sn_i^{\cdots\cdot}$ formed in the lattice cannot address the charge imbalance occurring on codoping in the present nanocrystals and requires lowering of some positive charge at the sites of the host cation. Thus, to fulfill the charge neutrality condition, there occurs a partial reduction of Sn^{x}_{Sn} to Sn''_{Sn}, as is evident from the occurrence of the 3d peak corresponding to SnO in the Sn 3d core-level spectra of Ni2 and Ni4 nanocrystals (Fig. 7) as well as the existence of local structures resembling SnO in the HR-TEM image of the Ni3 nanocrystals [Fig. 5(c)].

For the Co doped SnO_2 nanocrystals reported earlier,[22] Co was found to perturb the chemical environment of the Sn^{4+} in the nanocrystals.[22] However, in the present nanocrystals, on codoping with Ni, the core-level electronic configurations of all the three forms of Sn (Sn^{x}_{Sn}, $Sn_i^{\cdots\cdot}$, and Sn''_{Sn}) are not affected appreciably, as indicated by the absence of any significant chemical shift in the Sn 3d core-level spectra (Fig. 7) of the nanocrystals. Moreover, in the Co doped SnO_2 nanocrystals, on Co doping, only the point defect $Sn_i^{\cdots\cdot}$ appeared in the nanocrystals, and its concentration was found to increase with an increment in Co concentration.[22] However, interestingly, on Ni codoping, concentration of the point defect Sn''_{Sn} has been found to increase in compensation of $Sn_i^{\cdots\cdot}$ with an increase in Ni concentration (y), as shown in Fig. 14(a). The increment is such that for Ni0 nanocrystals, only $Sn_i^{\cdots\cdot}$ exist; for Ni2 nanocrystals, both the point defects—Sn''_{Sn} and $Sn_i^{\cdots\cdot}$ coexist in the lattice, whereas with increase in Ni concentration, for Ni4 nanocrystals, only Sn''_{Sn} remains along with Sn^{x}_{Sn} in the nanocrystals [Figs. 7 and 14(a)]. Thus, the charge neutrality condition in the lattice of the nanocrystals, which is deviated on increasing the Ni codoping concentration, as discussed earlier, is restored. However, the combined effect of the localized nature of these point defects in the lattice of the nanocrystals, the very small ratio of the defects $Sn_i^{\cdots\cdot}$ and Sn''_{Sn} to Sn^{x}_{Sn}, and the existence of local disorder of SnO in small average crystallite size of the nanocrystals make the SnO-resembling local structures to be directly nonobservable in the diffraction experiments—XRD (Fig. 1) and SAED [Fig. 5(b)] for the nanocrystals, but their effect, in conjunction with other point defects, can be observed, as discussed later.

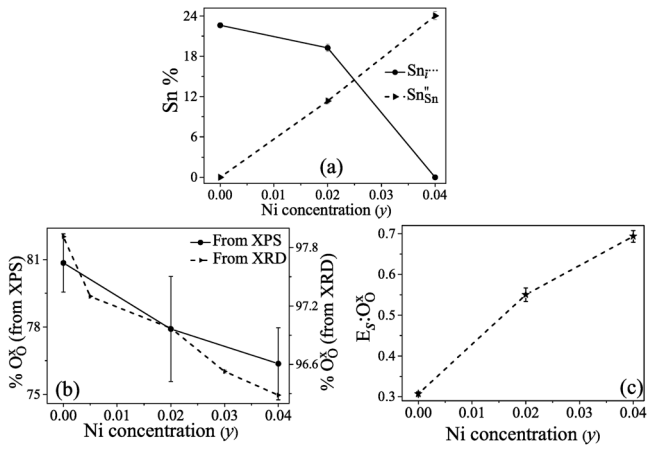

FIG. 14. Variation of % of $Sn_i^{\cdots\cdot}$ and Sn''_{Sn} in the total Sn concentration (a), % of lattice oxygen (O^x_O) as obtained from O 1s core-level XPS and Rietveld refinement of XRD spectra (b), and the ratio of the concentration of surface state to that of lattice oxygen (E_s : O^x_O) (c) with Ni doping concentration. All the solid and dotted lines are eye guides.

2. Stoichiometric anion Frenkel defect

In addition to the nonstoichiometric Sn related point defects—$Sn_i^{\cdots\cdot}$ and Sn''_{Sn}, there also exists O-related Frenkel-type stoichiometric point defects, i.e., oxygen vacancies (V_O) and oxygen interstitials (O_i) in the present nanocrystals. In fact, V_O is considered to be a very stable intrinsic point defect in SnO_2, for which SnO_2 is usually expressed in its nonstoichiometric form $SnO_{2-\delta}$.[6,7] The presence of V_O in the lattice of the nanocrystals can be perceived by comparing the 1s core level peak of O^x_O at ≈529.2 eV in the O 1s core-level spectra (Fig. 8) with the 3d core-level peak of Sn^{x}_{Sn} in the Sn 3d core-level spectra of the same nanocrystal, as well as from the Rietveld refinement of the XRD patterns (Fig. 1) for the nanocrystals. It can be seen that the concentration of V_O qualitatively increases with increase in Ni codoping concentration (y), as shown in Fig. 14(b). Now, V_O can have three charge states (charge with respect to the original lattice) — the neutral V_O (V^x_O), singly-ionized V_O ($V^{\cdot}_O$), and doubly-ionized V_O ($V^{\cdot\cdot}_O$). Among them, the only paramagnetic center is $V^{\cdot}_O$[29], and hence, only it can contribute to the paramagnetism in the nanocrystals. In fact, $V^{\cdot}_O$ is considered to enhance the ferromagnetic interactions in diluted magnetic oxide-semiconductor nanocrystals, as explained using the bound magnetic polaron model.[63] In the inset of Fig. 13, it can be seen that the Curie-Weiss fit predicts an antiferromagnetic interaction below 290 K for Ni0 nanocrystals whereas a ferromagnetic interaction for Ni3 nanocrystals. Hence, from this changeover of antiferromagnetic interactions to ferromagnetic interactions, it can be concluded that on increasing the Ni codoping concentration, the concentration of $V^{\cdot}_O$ increases in the nanocrystals and that they form the dominant point defect among all the charge states of V_O. The anion Frenkel counterpart of the V_O, i.e., the oxygen interstitials (O_i), is considered to relax to form dangling bonds as peroxide ion (O_2^{2-} and O^-) type structures,[6] which move to the surface of the nanocrystals to form surface defect states (E_s).[61] The existence

of these nonlattice oxygen, in the form of E_s, in the nanocrystals is evident from the occurrence of the peaks at higher binding energy (at ≈ 531.1 eV) to the peak for O_O^x in the O 1s core-level spectra for the nanocrystals (Fig. 8). Interestingly, the concentration of E_s has been found to increase with increase in Ni concentration (y), as can be observed from the qualitative increment in the ratio of E_s to O_O^x with y in Fig. 14(c). The simultaneous increment (qualitatively) in the concentration of V_O and E_s [Figs. 14(b) and 14(c), respectively] also clearly establishes the anion Frenkel-type nature of these oxygen-related point defects. This sort of similarity between these two anion Frenkel defects has also been observed for Co doped SnO_2 nanocrystals reported earlier, although the concentration of these defects decreased qualitatively with increase in Co doping.[22] However, as observed for Co doped SnO_2 nanocrystals that Co doping do not affect the chemical state of these anion Frenkel defects,[22] even on Ni codoping in the nanocrystals, the corresponding chemical states of these defects remain unperturbed in the present nanocrystals.

B. Microscopic influence of the point defects

As discussed earlier, the intrinsic point defects in the lattice of the present nanocrystals should play an important role in maintaining the tetragonal SnO_2 crystal structure (with space group $P4_2/mnm$) of the nanocrystals on Ni codoping. Now, distorted octahedral coordination geometry of Sn with O and the trigonal planar coordination geometry of O with Sn constitute an ideal tetragonal SnO_2 structure. Hence, it can be considered that the combined stoichiometric and nonstoichiometric point defects impact the coordination geometries for maintaining the tetragonal SnO_2 crystal structure throughout the Ni concentration. The microscopic influence of the point defects is concerned with the effect on the geometry of the Sn–O octahedron, as well as on the trigonal planar coordination geometry of O in the nanocrystals. This can be understood from the perspective of the effect of point defects on the bond parameters, i.e., bond lengths and bond angles. From Fig. 15, it can be seen that in the slightly distorted Sn–O octahedron with respect to the central atom Sn_{Sn}^x at (0.5, 0.5, 0.5) (viz., atom S1), four O_O^x, viz., atoms 1, 2, 5, and 6, lying on the two opposite *ab*-planes, are at the equatorial positions, each shared by two unit cells and two O_O^x, viz., atoms 3 and 4, lying completely inside the unit cell in two opposite planes parallel to *c*-axis, are at apical positions. For considering the trigonal planar coordination geometry of O, a typical O_O^x in Fig. 15, say, viz., atom 4, can be chosen, where the trigonal planar coordination geometry is formed along with Sn_{Sn}^x at positions, viz., S1, S2, and S3.

1. Effect on octahedral coordination geometry of Sn

In the complete Sn–O octahedron, there exists stoichiometric point defects $V_O^{\cdot}$, at specific positions, along with the Sn–O bonds, which are formed between the Sn (Sn_{Sn}^x and Sn_{Sn}'') and O_O^x of the octahedron. The effect on geometry formed by Sn–O bonds in the octahedron on codoping Ni can be understood based on the variation of the bond angle ∠1–S1–5, between O_O^x at 1 and 5 to Sn_{Sn} at S1 in Fig. 15. However, to explain this, the preferable position of the stoichiometric point defect $V_O^{\cdot}$ needs to be predetermined, which actually plays a crucial role in defining the geometry formed

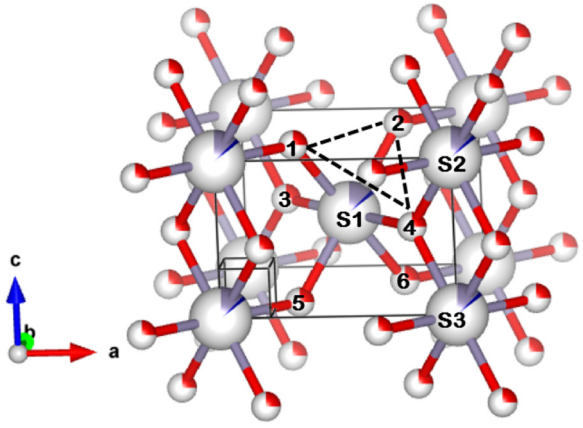

FIG. 15. The VESTA derived structure (using ball-and-stick model) for Ni3 nanocrystals. The atoms, viz., 1, 2, 3, 4, 5, and 6 denote the O_O^x and atom, viz., S denote the Sn_{Sn}^x lattice position. Atoms, viz., 1, 2, 3, 4, 5, and 6 form the 6 vertices of the central Sn–O octahedron. The dotted lines form Δ124 as one of the 8 triangular faces of the octahedron.

by the Sn–O bonds. Now, $V_O^{\cdot}$ can be created at an equatorial or apical position (Fig. 15). It can be observed from Fig. 16(a) that ∠1–S1–3, ∠3–S1–5 always remain at 90° throughout the Ni concentration. Similar is the case for ∠2–S1–4 and ∠4–S1–6. This would not have been, if $V_O^{\cdot}$ is created at the equatorial position, i.e., at, say, position 1 or 2, because in that case, the only repulsion between O_O^x at positions, viz., 3 and 5 or between 4 and 6 would have increased the bond angle greater than 90°. Thus, it can be safely assumed that $V_O^{\cdot}$ is preferably created at the apical position in the octahedron. Due to the $V_O^{\cdot}$ being created at an apical position, the size of the lattice site with respect to the site having O_O^x in original lattice reduces; hence, the apical bond length must decrease with increment in Ni codoping concentration (y), as shown in Fig. 16(b). Now, the nonstoichiometric point defect Sn_{Sn}'' would be created at the cationic lattice sites either, viz., S1, S2, or S3. Since the ionic radius of Sn_{Sn}'' (≈ 1.18 Å) is larger than that of Sn_{Sn}^x (≈ 0.69 Å), the size of a cationic lattice site (viz., S1, S2, or S3 in Fig. 15) increases due to the formation of Sn_{Sn}''. Considering the cationic lattice site, viz., S1 in Fig. 15, when its size increases, the intersite distance between sites, viz., S1 and 1, S1 and 2, S1 and 5, or S1 and 6, effectively increases. This, along with the creation of $V_O^{\cdot}$ at an apical position leads to an outward relaxation of the three nearest neighbor Sn_{Sn}^x,[15] which eventually increases the equatorial bond length with increase in Ni concentration (y) [Fig. 16(b)]. As such, the electron density on the central cationic site decreases, i.e., the polarization of the bond decreases, thereby reducing the covalent character of the Sn–O bond.[64] Thus, in a combined effect of reduction in the electron density on the cationic site, as well as reduction in the net effective repulsion between the equatorial O_O^x pairs on the two opposite *ab*-planes, i.e., of viz., atom 1 with atom 5 and atom 2 with atom 6 as compared to that between the equatorial O_O^x pairs on the same *ab*-plane, i.e., of viz., atom 1 with atom 2 and atom 5 with atom 6, due to $V_O^{\cdot}$ being created at an apical position, the bond angles ∠1−S1−5 = ∠2−S1−6 effectively decrease [Fig. 16(c)], whereas the

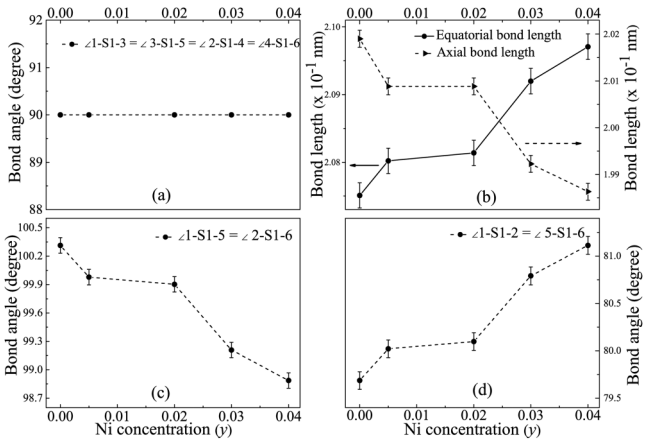

FIG. 16. The variation of various Sn–O bond parameters, in Sn octahedral coordination geometry, with Ni codoping concentration (y). The solid and dotted lines are eye guides.

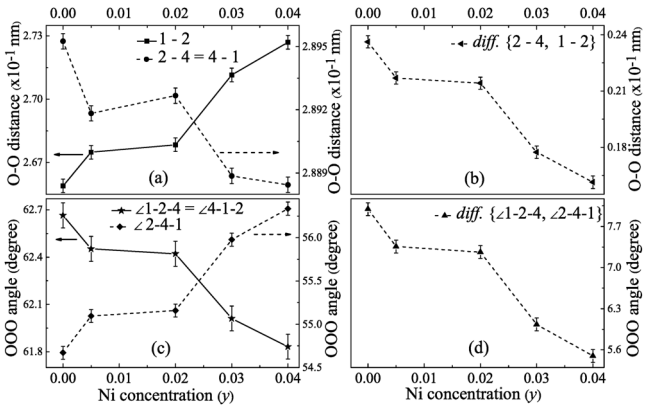

FIG. 17. The variation of various O–O bond parameters with Ni codoping concentration (y). The syntax *diff* {*quantity1*,*quantity2*} stands for the difference between *quantity1* and *quantity2*. The solid and dotted lines are eye guides.

bond angles $\angle 1{-}S1{-}2 = \angle 5{-}S1{-}6$ [Fig. 16(d)] effectively increase, with increase in Ni concentration. As such, the equatorial oxygen atom pairs at, viz., 1 and 5 or 2 and 6, might leave the *ab*-planes to come closer to each other for a more compact and stable geometry. Thus, the resultant geometry, formed by the Sn–O bonds, resembles a distorted tetrahedron, like SnO.[7] These Sn–O bonds, in combination with the stoichiometric point defects $V_O^{\cdot}$ (preferably created at the apical positions in Fig. 15), form the complete distorted octahedral geometry of Sn. Now, by geometry, a regular octahedron is built up of six equilateral triangles. Thus, when a distortion in the octahedron occurs, a distortion in each of the equilateral triangle can be expected. Such a typical triangle $\triangle 1{-}2{-}4$ can be considered in Fig. 15, shown by dotted lines, formed by the O_O^x, viz., 1, 2, and $V_O^{\cdot}$, viz., 4, at the vertices. For the triangle to be an equilateral triangle, distance $1-2 = 2-4 = 4-1$ and $\angle 1{-}2{-}4 = 60^\circ = \angle 2{-}4{-}1 = \angle 4{-}1{-}2$. As discussed above, under the combined effect of the creation of the nonstoichiometric point defect Sn_{Sn}'' at the cationic site and the stoichiometric point defect $V_O^{\cdot}$, created at an apical position, the bond angles $\angle 1{-}S1{-}2 = \angle 5{-}S1{-}6$ [Fig. 16(d)] effectively increase, with increase in Ni concentration. This increases the distance between the equatorial O_O^x on the same *ab* plane, i.e., the distance 1–2 of $\triangle$ 1–2–4 in Fig. 15 and reduces the distance $2{-}4 = 4{-}1$, with increase in y [Fig. 17(a)]. As such, the $\angle 1{-}2{-}4 = \angle 4{-}1{-}2$ decreases, whereas the $\angle 2{-}4{-}1$ increases, with increase in y [Fig. 17(c)]. However, from Figs. 17(b) and 17(d), it can be observed that the variation of the edge lengths and angles of the $\triangle 1{-}2{-}4$ in Fig 15 is such that the difference between 2–4(=4–1) and 1–2 and that between $\angle 1{-}2{-}4(=\angle 4{-}1{-}2)$ and $\angle 2{-}4{-}1$ decrease with increase in Ni concentration (y), indicating that the isosceles triangle $\triangle 1{-}2{-}4$ tends to an equilateral triangle with increasing y; i.e., Ni codoping in $Sn_{0.97}Co_{0.03}O_2$ nanocrystals leads to a decrease in the distortion of the complete Sn–O octahedron, when all the Sn–O bonds and the point defects — $V_O^{\cdot}$ and Sn_{Sn}'' — are simultaneously considered.

Hence, it can be concluded that the creation of point defects $V_O^{\cdot}$ at the apical position and Sn_{Sn}'' on Ni codoping affects the distorted Sn–O octahedral geometry in a way that the octahedral distortion reduces. However, if the geometry formed by the Sn–O bonds is considered, then they seem to form a distorted tetrahedral geometry, mimicking SnO, from the existing distorted octahedral geometry of SnO_2 with no such point defects. The formation of local SnO-resembling structures is also confirmed from HR-TEM, where lattice spacing corresponding to (111) and (112) lattice planes of the orthorhombic SnO phase has been observed, along with (110) planes of the tetragonal SnO_2 phase [Fig. 5(c)]. The stable multivalence nature of Sn supports this coexistence of SnO and SnO_2 phases in the nanocrystals.[6,7]

2. Effect on trigonal planar coordination geometry of O

By geometry, a trigonal planar coordination geometry is formed by four atoms — a central atom and three similar atoms at the periphery, all four lying on the same plane, with all the three bond lengths being equal and all the bond angles being equal to 120°. Figure 18 shows the variation of the bond lengths and angles for the trigonal planar coordination geometry of a typical O_O^x at the position, viz., atom 4 in Fig. 15. It can be seen that the bond length $S2{-}4 = S3{-}4 \neq S1{-}4$ [Fig. 18(a)] and the bond angle $\angle S1{-}4{-}S2 = \angle S3{-}4{-}S1 \neq \angle S2{-}4{-}S3$ [Fig. 18(c)]. Thus, there lies a distortion in the trigonal planar coordination geometry. With Ni codoping, since the overall electronic polarization of bond decreases, the bond angle $\angle S2{-}4{-}S3$ decreases, with an increase in $\angle S1{-}4{-}S2 = \angle S3{-}4{-}S1$. The change in bond lengths and bond angles occurs in a way that the difference between the bond lengths S2–4(= S3–4) and S1–4 as well as that between bond lengths $\angle S1-4-S2$ ($= \angle S3{-}4{-}S1$) and $\angle S2{-}4{-}S3$ increases with increase in Ni codoping concentration (y) [Figs. 18(b) and 18(d), respectively]. Hence, it can be concluded that Co-Ni

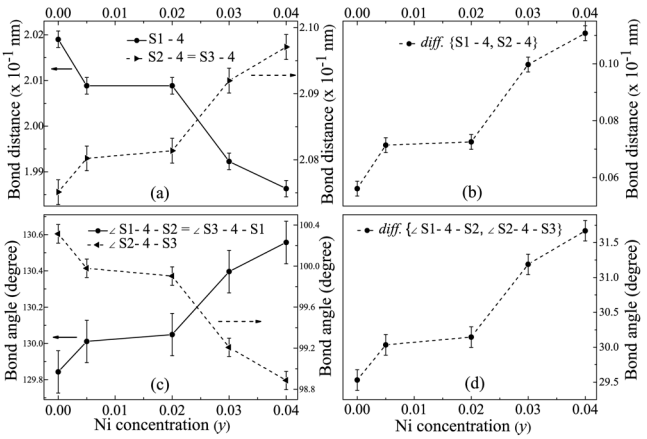

FIG. 18. The variation of various Sn–O bond parameters, in the trigonal planar coordination geometry of O, with Ni codoping concentration (y). The syntax *diff* {*quantity1*,*quantity2*} stands for the difference between *quantity1* and *quantity2*. The solid and dotted lines are eye guides.

codoping leads to an enhancement of the distortion of trigonal planar coordination geometry of O in SnO_2 nanocrystals.

C. Macroscopic influence of the point defects

Based on the above discussed effects of the stoichiometric and nonstoichiometric intrinsic point defects on the coordination geometries of the tetragonal SnO_2 structure of the nanocrystals, the macroscopic effect of the point defects on the structural properties of the nanocrystals can be elaborated. On increasing the Ni codoping concentration, the concentration of the point defect Sn''_{Sn} and $V_O^{\cdot}$ increases in the lattice of the nanocrystals [Figs. 14(a) and 14(b), respectively]. Since Sn''_{Sn} has a higher ionic radius (≈ 1.18 Å) as compared to that of Sn^x_{Sn} (≈ 0.69 Å), it counterbalances the ionic radius mismatch between the codopants Co and Ni with respect to that of host Sn^x_{Sn}. Moreover, each Sn''_{Sn} has two units of positive charge lower than that of Sn^x_{Sn}, which lowers the effective positive charge at the host lattice site in the nanocrystals. This, along with the point defect $V_O^{\cdot}$, balances the ionic charges in the lattice of the nanocrystals. Thus, both the ionic radius and charge neutrality criteria become stabilized, which allows the nanocrystals to retain the tetragonal SnO_2 crystal structure throughout the Ni concentration, as can be observed from Fig. 1. This stabilization of crystal structure on Co and Ni codoping in the SnO_2 nanocrystals is much more effective than that can be obtained by only Co doping, since on Co doping, no such point defects have been introduced in the lattice, which can counterbalance the ionic radius mismatch and violation of charge neutrality on Co doping.[22] As such, higher substitution of Sn^x_{Sn} with dopants can be done in the present Co and Ni codoped SnO_2 nanocrystals as compared to that only for Co doped SnO_2 nanocrystals. However, due to changes in the geometry of the Sn–O octahedron and the trigonal planar coordination geometry of O as a result of inclusion of Sn''_{Sn} and $V_O^{\cdot}$ on Ni codoping, overall distortion in the lattice increases, as evident from the increase in the parameter E_0 in the Urbach-type absorption with increase in y [Fig. 10(f)]. Considering Fig. 15, due to larger ionic radius of the point defect Sn''_{Sn} as compared to Sn^x_{Sn}, and $V_O^{\cdot}$ being created at an apical position, the covalent character of the Sn–O bond reduces, as discussed earlier. This effectively decreases the bond angle $\angle 1{-}S1{-}5 = \angle 2{-}S1{-}6$ [Fig. 16(c)] and increases the bond angles $\angle 1{-}S1{-}2 = \angle 5{-}S1{-}6$ [Fig. 16(d)]. Hence, the lattice parameter a qualitatively increases, whereas c qualitatively decreases with increase in Ni concentration, as observed in Figs. 4(a) and 4(b). The variation of lattice parameters a and c deviates from Vegard's law, which is expected since for conforming to Vegard's law, the host and the dopant need to have negligible disparity in the ionic sizes and electrochemical differences,[65] which is not valid in the present nanocrystals. The corresponding increase in the unit cell volume ($V = a^2c$), as shown in Fig. 4(c), is reflected in an enhancement of the average tensile lattice strain [inset (a) of Fig. 3], with an increase in d_{hkl}, e.g., d_{110} as shown in the inset (b) of Fig. 3. On the other hand, an opposite trend was observed for Co doped SnO_2 nanocrystals.[22] Thus, due to the combined effect of the stoichiometric and nonstoichiometric point defects, formed in the lattice of the Co doped SnO_2 nanocrystals (i.e., $y = 0.00$) on codoping with Ni, increases the possibility of the nanocrystals for applications as anodes of lithium ion batteries, which can facilitate intercalation of Li ions during charging-discharging cycles.[66]

An interesting effect of the stoichiometric point defects on the emission properties of the nanocrystals can be observed from the variation of spectral contribution of blue luminescence with Ni concentration as shown in Fig. 12(a). The presence of all the emissions below $E_g^{allw.}$ of the nanocrystals (Fig. 11) suggests the inclusion of defect trap states in the sub-bandgap region, which act as trapping centers for the electrons relaxing from the conduction band. It has been proposed that among the possible point defects in SnO_2, only V_O forms energy levels below the conduction band minimum (CBM).[7] Now, as discussed above, for the present nanocrystals, V_O has been found to exist as the stoichiometric anion Frenkel defect $V_O^{\cdot}$, the concentration of which has been found to increase with increase in y [Fig. 14(b)]. Also, the concentration of the surface defect states, E_s, which form the Frenkel counterpart of $V_O^{\cdot}$, has been found to increase with Ni codoping concentration, as shown in Fig. 14(c). Kar *et al.*[61] and Gu *et al.*[62] proposed the role of E_s along with $V_O^{\cdot}$ centers for the origin of blue luminescence in SnO_2 nanocrystals, whereas, Zhou *et al.*[60] proposed the transition of electrons from CBM to E_s for the observed blue emission in the SnO_2 nanocrystals. The origin of the blue luminescence for the present $Sn_{0.97-y}Co_{0.03}Ni_yO_2$ nanocrystals can be due to a combination of both the mechanisms proposed above, following the schematic energy level diagram adopted earlier.[22] Thus, a direct effect of the increase in the concentrations of stoichiometric anion Frenkel point defects in these nanocrystals is an enhancement of the spectral contribution of blue luminescence by ≈72.33%, as shown in Fig. 12(a). This increment is highly fascinating, since Co doping does not have an appreciable effect on the spectral contribution of blue luminescence as reported earlier for Co doped SnO_2 nanocrystals.[22] Thus, codoping with Ni renders the Co doped SnO_2 nanocrystals (i.e., $y = 0.00$) to be a potential material for blue light emitting diodes. The green luminescence, on the other hand, involves the transition of electrons from V_O^x to E_s and $V_O^{\cdot\cdot}$/ $V_O^{\cdot}$.[22]

Therefore, a higher concentration of $V_O^{\cdot}$ should decrease the contribution of the green emission to the total PL spectrum. The PL spectra shown in Fig. 12(b) are consistent with this hypothesis. Further investigations into the decrease in the green emission features could shed further light on this mechanism.

V. SUMMARY AND CONCLUSIONS

Cobalt, nickel codoped SnO_2 nanocrystals ($Sn_{0.97-y}Co_{0.03}Ni_yO_2$; $0.00 \leq y \leq 0.04$) have been successfully prepared via the chemical coprecipitation technique. Although both nonstoichiometric and anion Frenkel-type stoichiometric point defects have been found to exist in the nanocrystals doped only with Co, codoping Ni into these nanocrystals has a profound effect on the intrinsic point defects. However, unlike for only Co doping, on increasing the Ni codoping concentration, the already existing nonstoichiometric defect of $Sn_i^{\cdots}$ is systematically converted to Sn''_{Sn}, and the anion Frenkel defects, $V_O^{\cdot}$ and O_i, manifested in the form of E_s, have also been found to increase with Ni codoping concentration. The combined effects of the stoichiometric $V_O^{\cdot}$ and nonstoichiometric Sn''_{Sn} point defects formed due to Co and Ni codoping in SnO_2 nanocrystals have been observed on the structural properties of these nanocrystals. Firstly, it stabilizes the crystal structure of the nanocrystals on Co and Ni codoping in a much more effective way than that can be obtained by only Co doping in the SnO_2 nanocrystals. This allows for higher substitution of Sn_{Sn}^x with dopants on Co and Ni codoping as compared to that only for Co doped SnO_2 nanocrystals. Secondly, the lattice parameter a qualitatively increases, whereas c qualitatively decreases with increase in Ni concentration. The corresponding increase in the unit cell volume is reflected in an enhancement of the average tensile lattice strain, with an increase in d_{hkl}, in contrast to that for only Co doped SnO_2 nanocrystals, thereby opening the possibility of the nanocrystals, on codoping with Ni, for applications as anodes of lithium ion batteries. A fascinating effect of the stoichiometric point defects on the emission properties of the nanocrystals has been an enhancement of the spectral contribution of blue luminescence by $\approx 72.33\%$ for the $Sn_{0.93}Co_{0.03}Ni_{0.04}O_2$ nanocrystals as compared to that observed for $Sn_{0.97}Co_{0.03}O_2$ nanocrystals, thereby making the codoped nanocrystals as a potential material for blue light emitting diodes.

SUPPLEMENTARY MATERIAL

See the supplementary material for the peak parameters of the deconvoluted peaks [as per Eq. (5)] in the photoluminescence spectra of the $Sn_{0.97-y}Co_{0.03}Ni_yO_2$ (with $0.00 \leq y \leq 0.04$) nanocrystals.

ACKNOWLEDGMENTS

S.R. acknowledges CSIR, India for the Senior Research Fellowship vide File No. 09/013(0849)/2018—EMR-I. A.K.G. acknowledges the DST-FIST, DST-PURSE, UGC-UPE, and UGC-CAS programs. A.K.G. also acknowledges DAE-BRNS, India (Grant No. 2011/37P/11/BRNS/1038-1); CSIR, India [Grant No. 03(1302)/13/EMR-II]; and UGC, India [Grant No. F: 42-787/2013 (SR)] for financial support and acknowledges the Bio-Physics Lab, Department of Physics (BHU) for the PL facility; the Laboratory for Central Facilities, Department of Physics (BHU) for VSM based room temperature magnetization measurements; and the Central Instrument Facility, IIT-BHU for SQUID based temperature dependent magnetization measurements.

REFERENCES

[1]H. Y. Peng, Y. F. Li, W. N. Lin, Y. Z. Wang, X. Y. Gao, and T. Wu, Sci. Rep. **2**, 442 (2012).
[2]T. Fukumura, Y. Yamada, H. Toyosaki, T. Hasegawa, H. Koinuma, and M. Kawasaki, Appl. Surf. Sci. **223**, 62 (2004).
[3]J. Jiang, Y. Lu, B. K. Meyer, D. M. Hofmann, and M. Eickhoff, J. Appl. Phys. **119**, 245703 (2016).
[4]Y. Li, W. Yin, R. Deng, R. Chen, J. Chen, Q. Yan, B. Yao, H. Sun, S.-H. Wei, and T. Wu, NPG Asia Mater. **4**, e30 (2012).
[5]F. Mei, H. Shen, L. Li, G. Zang, Y. Shao, L. Liu, L. Lei, F. Huang, X. Lu, and J. Zhu, J. Appl. Phys. **125**, 074502 (2019).
[6]K. G. Godinho, A. Walsh, and G. W. Watson, J. Phys. Chem. C **113**, 439 (2009).
[7]C. Kılıc and A. Zunger, Phys. Rev. Lett. **88**, 095501 (2002).
[8]K. Chopra, S. Major, and D. Pandya, Thin Solid Films **102**, 1 (1983).
[9]B. Stjerna, E. Olsson, and C. G. Granqvist, J. Appl. Phys. **76**, 3797 (1994).
[10]K. B. Sundaram and G. K. Bhagavat, J. Phys. D Appl. Phys. **16**, 69 (1983).
[11]C. Terrier, J. Chatelon, R. Berjoan, and J. Roger, Thin Solid Films **263**, 37 (1995).
[12]S. Samson and C. G. Fonstad, J. Appl. Phys. **44**, 4618 (1973).
[13]F. Kroger and H. H. J. Vink, Solid State Phys. **3**, 307 (1956).
[14]C. Kılıc and A. Zunger, Appl. Phys. Lett. **81**, 73 (2002).
[15]A. K. Singh, A. Janotti, M. Scheffler, and C. G. Van de Walle, Phys. Rev. Lett. **101**, 055502 (2008).
[16]W. M. Hlaing Oo, S. Tabatabaei, M. D. McCluskey, J. B. Varley, A. Janotti, and C. G. Van de Walle, Phys. Rev. B **82**, 193201 (2010).
[17]F. Bekisli, M. Stavola, W. B. Fowler, L. Boatner, E. Spahr, and G. Lüpke, Phys. Rev. B **84**, 035213 (2011).
[18]J. Buckeridge, C. R. A. Catlow, M. R. Farrow, A. J. Logsdail, D. O. Scanlon, T. W. Keal, P. Sherwood, S. M. Woodley, A. A. Sokol, and A. Walsh, Phys. Rev. Mater. **2**, 054604 (2018).
[19]N. Kikuchi, A. Samizo, S. Ikeda, Y. Aiura, K. Mibu, and K. Nishio, Phys. Rev. Mater. **1**, 021601 (2017).
[20]S. B. Ogale, R. J. Choudhary, J. P. Buban, S. E. Lofland, S. R. Shinde, S. N. Kale, V. N. Kulkarni, J. Higgins, C. Lanci, J. R. Simpson, N. D. Browning, S. Das Sarma, H. D. Drew, R. L. Greene, and T. Venkatesan, Phys. Rev. Lett. **91**, 077205 (2003).
[21]K. C. Verma and R. K. Kotnala, Phys. Chem. Chem. Phys. **18**, 17565 (2016).
[22]S. Roy, A. G. Joshi, S. Chatterjee, and A. K. Ghosh, Nanoscale **10**, 10664 (2018).
[23]A. Ahmed, T. Ali, M. Naseem Siddique, A. Ahmad, and P. Tripathi, J. Appl. Phys. **122**, 083906 (2017).
[24]K. Srinivas, S. M. Rao, and P. V. Reddy, Nanoscale **3**, 642 (2011).
[25]P. I. Archer and D. R. Gamelin, J. Appl. Phys. **99**, 08M107 (2006).
[26]T. Sabergharesou, T. Wang, L. Ju, and P. V. Radovanovic, Appl. Phys. Lett. **103**, 012401 (2013).
[27]S. Ghosh, D. D. Munshi, and K. Mandal, J. Appl. Phys. **107**, 123919 (2010).
[28]S. J. Gilliland, J. A. Sans, J. F. Sánchez-Royo, G. Almonacid, B. García-Domene, A. Segura, G. Tobias, and E. Canadell, Phys. Rev. B **86**, 155203 (2012).
[29]S. Das, S. Kar, and S. Chaudhuri, J. Appl. Phys. **99**, 114303 (2006).
[30]A. Bouaine, N. Brihi, G. Schmerber, C. Ulhaq-Bouillet, S. Colis, and A. Dinia, J. Phys. Chem. C **111**, 2924 (2007).
[31]K. Srinivas, M. Vithal, B. Sreedhar, M. M. Raja, and P. V. Reddy, J. Phys. Chem. C **113**, 3543 (2009).
[32]R. D. Shannon, Acta Crystallogr. A **32**, 751 (1976).
[33]J. Okabayashi, S. Kono, Y. Yamada, and K. Nomura, J. Appl. Phys. **112**, 073917 (2012).
[34]S. Nakamura, T. Mukai, and M. Senoh, Jpn. J. Appl. Phys. **30**, L1998 (1991).
[35]K. Nomura, J. Okabayashi, K. Okamura, and Y. Yamada, J. Appl. Phys. **110**, 083901 (2011).

[36]K. Subramanyam, N. Sreelekha, D. A. Reddy, G. Murali, B. Poornaprakash, S. Ramu, and R. Vijayalakshmi, Solid State Sci. **39**, 74 (2015).
[37]K. Subramanyam, N. Sreelekha, D. A. Reddy, G. Murali, and R. Vijayalakshmi, Superlattices Microstruct. **82**, 207 (2015).
[38]S. Bhuvana, H. B. Ramalingam, G. Thilakavathi, and K. Vadivel, Mater. Technol. **32**, 305 (2017).
[39]R. Khan, Zulfiqar, S. Fashu, and M.-U. Rahman, J. Mater. Sci. Mater. Electron. **27**, 7725 (2016).
[40]N. Ahmad and S. Khan, J. Alloys Compd. **720**, 502 (2017).
[41]N. Bhakta and P. K. Chakrabarti, Appl. Phys. A **125**, 73 (2019).
[42]J. M. D. Coey, M. Venkatesan, and C. B. Fitzgerald, Nat. Mater. **4**, 173 (2005).
[43]J. Hays, A. Punnoose, R. Baldner, M. H. Engelhard, J. Peloquin, and K. M. Reddy, Phys. Rev. B **72**, 075203 (2005).
[44]G. A. Alanko, A. Thurber, C. B. Hanna, and A. Punnoose, J. Appl. Phys. **111**, 07C321 (2012).
[45]S. Kumar, S. Basu, B. Rana, A. Barman, S. Chatterjee, S. N. Jha, D. Bhattacharyya, N. K. Sahoo, and A. K. Ghosh, J. Mater. Chem. C **2**, 481 (2014).
[46]E. Prince and J. Stalick, NIST Special Publication, Vol. 597, 1992.
[47]H. Kimura, T. Fukumura, M. Kawasaki, K. Inaba, T. Hasegawa, and H. Koinuma, Appl. Phys. Lett. **80**, 94 (2002).
[48]W. Zhou and H. F. Greer, Eur. J. Inorg. Chem. **2016**, 941.
[49]D. Su, Green Energy Environ. **2**, 70 (2017).
[50]A. Naumkin, A. Vass, S. Gaarenstroom, and C. Powell, see http://srdata.nist.gov/xps/ for "NIST Standard Reference Database 20," Version 4.1.
[51]J. Moulder and J. Chastain, *Handbook of X-ray Photoelectron Spectroscopy: A Reference Book of Standard Spectra for Identification and Interpretation of XPS Data* (Physical Electronics Division, PerkinElmer Corporation, 1992).
[52]D. Fröhlich, R. Kenklies, and R. Helbig, Phys. Rev. Lett. **41**, 1750 (1978).
[53]V. T. Agekyan, Phys. Status Solidi A **43**, 11 (1977).
[54]J. Tauc, *Amorphous and Liquid Semiconductors* (Plenum, New York, 1974), Chap. 4
[55]F. Urbach, Phys. Rev. **92**, 1324 (1953).
[56]J. Pankove, *Optical Processes in Semiconductors* (Dover, New York, 1975).
[57]A. K. Ghosh, K. K. Som, S. Chatterjee, and B. K. Chaudhuri, Phys. Rev. B **51**, 4842 (1995).
[58]S. John, C. Soukoulis, M. H. Cohen, and E. N. Economou, Phys. Rev. Lett. **57**, 1777 (1986).
[59]M. Nagasawa and S. Shionoya, Solid State Commun. **7**, 1731 (1969).
[60]X. T. Zhou, F. Heigl, M. W. Murphy, T. K. Sham, T. Regier, I. Coulthard, and R. I. R. Blyth, Appl. Phys. Lett. **89**, 213109 (2006).
[61]A. Kar, S. Kundu, and A. Patra, J. Phys. Chem. C **115**, 118 (2011).
[62]F. Gu, S. F. Wang, M. K. Lü, G. J. Zhou, D. Xu, and D. R. Yuan, J. Phys. Chem. B **108**, 8119 (2004).
[63]B. Prajapati, S. Roy, S. Sharma, A. G. Joshi, S. Chatterjee, and A. K. Ghosh, Phys. Status Solidi B **256**, 1800262 (2019).
[64]K. Fajans, Naturwissenschaften **11**, 165 (1923).
[65]A. R. Denton and N. W. Ashcroft, Phys. Rev. A **43**, 3161 (1991).
[66]J. S. Chen and X. W. D. Lou, Small **9**, 1877 (2013).